


Receiver operating characteristic curves for a simple stochastic process that carries a static signalDavide Bernardi * and Benjamin Lindner*Bernstein Center for Computational Neuroscience Berlin, 10115 Berlin, Germany
and Physics Department of Humboldt University Berlin, 12489 Berlin, Germany*(Received 17 April 2020; revised manuscript received 13 May 2020; accepted 14 May 2020;
published 18 June 2020)

The detection of a weak signal in the presence of noise is an important problem that is often studied in terms of the receiver operating characteristic (ROC) curve, in which the probability of correct detection is plotted against the probability for a false positive. This kind of analysis is typically applied to the situation in which signal and noise are stochastic variables; the detection problem emerges, however, also often in a context in which both signal and noise are stochastic processes and the (correct or false) detection is said to take place when the process crosses a threshold in a given time window. Here we consider the problem for a combination of a static signal which has to be detected against a dynamic noise process, the well-known Ornstein-Uhlenbeck process. We give exact (but difficult to evaluate) quadrature expressions for the detection rates for false positives and correct detections, investigate systematically a simple sampling approximation suggested earlier, compare to an approximation by Stratonovich for the limit of high threshold, and briefly explore the case of multiplicative signal; all theoretical results are compared to extensive numerical simulations of the corresponding Langevin equation. Our results demonstrate that the sampling approximation provides a reasonable description of the ROC curve for this system, and it clarifies limit cases for the ROC curve.

DOI: [10.1103/PhysRevE.101.062132](https://doi.org/10.1103/PhysRevE.101.062132)**I. INTRODUCTION**

Living organisms often face the problem of detecting the presence of a signal in a noisy background. In solving this task, they can make two possible mistakes: They either react although no signal is present, which is a *false positive*, a false alarm, or a so-called type I error, or they do not react when the signal was there, which is a *miss*, or type II error. The likelihood of both error types is influenced by how sensitive the reaction criterion is or, in other words, on how high the decision threshold is. The consequences of each kind of error depend on the context so that, in general, finding an optimal sensitivity threshold for a detection procedure or equipment can be challenging, a problem that was first formally analyzed in the context of radio engineering [1].

The standard way of representing the trade-off between sensitivity and specificity of the detector's response is the *receiver operating characteristic* (ROC) curve [2–5]. It was introduced for a military purpose, that is, to study the performance of radar receivers [6], and since then it has found wide application in classification problems in the most diverse contexts, including medical physics [7,8], stochastic nonlinear systems [9–12], experimental and theoretical neuroscience [13–16], analysis of earthquake occurrence [17,18], network structure and function [19–24], and gravitational wave detection [25–27].

Since the earlier works, a pillar of most analytical approaches is represented by the Gaussian channel, in which the noise that obfuscates the signal is Gaussian, white (temporally

uncorrelated), and simply added to the signal. The centrality of the Gaussian channel cannot be surprising considering its pivotal role in Shannon's information theory [28] as detecting the presence of a signal can indeed be viewed as transmitting one single bit of information. Although the fast thermal noise emerging in artificial detectors can in most situations be approximated as white, in neural signal detection, for instance, distracting fluctuations often display pronounced temporal correlations stemming, for instance, from synaptic filtering [29,30], slow channel noise [31,32], or network interactions [33–36].

Although colored (temporally correlated) Gaussian noise has indeed been studied in the context of optimal Neyman-Pearson detectors [3,5,10], here we investigate analytically a different detection problem in which the signal is static, the noise is temporally correlated, and the detector is triggered instantly when a fixed threshold is reached. However, the detector is only active in a finite time window, so that the time dependence cannot be ignored.

The noise process we consider in this study is the Ornstein-Uhlenbeck (OU) process, a prototypical stochastic process that has been the subject of illustrious scientific papers [37,38] and chapters in distinguished textbooks [39,40]. Building on classic results, we are able to derive an exact analytical solution for the ROC curve. Unfortunately, this exact expression involves the numerical evaluation of nested integrals of special functions, which proves very challenging, and renders this solution impractical. However, we show that a sampling approximation, which is conceptually simple and easy to compute, yields a reasonably accurate estimate for all parameters. Due to this analytical approximation, we can fully characterize the system and infer the limiting behavior for

*Corresponding author: davide.bernardi@bccn-berlin.de

infinitely long observation time: in this limit, perfect detection of an arbitrarily weak signal is possible. Furthermore, we show how our findings relate to a result by Stratonovich [41], which is valid in the limit of high detection threshold, and we briefly explore how our results can be extended to the situation in which the signal affects the noise intensity instead of the mean. Preliminary results indicate that the proposed approximation can also be applied to a generic stationary Gaussian process if its autocorrelation function is known.

II. MODEL AND DEFINITIONS

Let $\hat{x}(t)$ be an OU process subject to a static offset s . The time evolution of $\hat{x}(t)$ is [37,38]

$$\tau_c \dot{\hat{x}}(t) = -\hat{x}(t) + s + \sqrt{2\sigma_{\hat{x}}^2 \tau_c} \xi(t), \quad (1)$$

where τ_c is the autocorrelation time of the process, $\sigma_{\hat{x}}^2$ its stationary variance, and $\xi(t)$ is Gaussian white noise with zero mean and unit intensity. In other words, if averaging over trials is indicated by angular brackets, then $\langle \xi(t) \rangle = 0$ and $\langle \xi(t)\xi(t') \rangle = \delta(t - t')$.

In our interpretation of the equation, the additive offset s carries a static signal, which can be present ($s \neq 0$) or absent ($s = 0$), depending on the trial. In both cases, we assume that the system had enough time to reach the equilibrium, i.e., we assume that the probability to find the process at a particular value of \hat{x} is given by the stationary probability distribution, which will depend on the parameters of the system ($\tau_c, \sigma_{\hat{x}}^2$) and on the presence or absence of the signal.

To detect the signal, a simple threshold detector active for a given time window \hat{T} is employed. The precise definition of the working principle of the detector is given below. First, it is convenient to rescale time in units of τ_c and the displacement from the origin of \hat{x} in units of $\sigma_{\hat{x}}$. We will indicate the rescaled process by $x(t)$, which evolves according to

$$\dot{x}(t) = -x(t) + \delta + \sqrt{2}\xi(t), \quad (2)$$

where $\delta = s/\sigma_{\hat{x}}$. Furthermore, let us define $T = \hat{T}/\tau_c$, i.e., the time window in units of the correlation time. In this way, the total number of parameters determining the system is reduced from 4 ($s, \sigma_{\hat{x}}, \hat{T}, \tau_c$) to 2 (δ, T). We note that the absolute value of δ can be regarded as a signal-to-noise ratio (SNR); however, δ itself is not an SNR in general because it can be negative (a case that will briefly be addressed below for completeness). For the main part of this study $\delta > 0$, and in this case the reader is not mistaken to think of δ as an SNR.

The numerical simulation of Eq. (2) will be performed by using a simple Euler integration scheme, i.e., for $x_\ell = x(t_\ell) = x(t_0 + \ell \Delta t)$

$$x_{\ell+1} = x_\ell(1 - \Delta t) + \delta \Delta t + \sqrt{2\Delta t} \eta_\ell, \quad (3)$$

where η_ℓ are independent Gaussian numbers with zero mean and unit variance, i.e., $\langle \eta_\ell \rangle = 0$ and $\langle \eta_\ell \eta_k \rangle = \delta_{\ell,k}$, and we will use an integration time step of $\Delta t = 10^{-4}$ for all numerical examples. To obtain each numerically measured ROC curve in this study, we will evaluate Eq. (3) from the initial to the final point (i.e., for $N_{\text{steps}} = T/\Delta t$ time steps) and repeat the simulation of each trajectory $N_{\text{trials}} = 2 \times 10^6$ times. This large number of simulated trajectories should yield an accurate numerical estimate of the true ROC curve, except for values

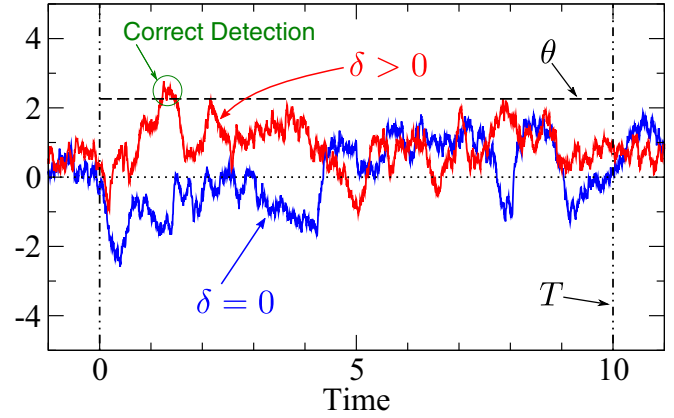


FIG. 1. Illustration of the system considered in this study. One realization of the process in the presence of the signal and one realization of the process in the absence of the signal are shown (the two lines are joined by arrows to their labels). The detector responds whenever the threshold θ (dashed line) is exceeded at least once within the detection time window $(0, T)$ (dotted vertical lines). If such an event occurs in the presence of the signal, then a correct detection event is registered, as in this case. If $x(t)$ exceeds the threshold for $\delta = 0$, then a false positive is recorded for the corresponding trial. Trajectories were simulated according to Eq. (3). Parameters: $\delta = 1.0$ and $T = 10$.

extremely close to zero or 1. The initial point is drawn from the stationary distribution $P_0(x - \delta)$, where $P_0(x)$ is defined in Eq. (13) below.

The detector works as depicted in Fig. 1: It responds whenever $x(t)$ exceeds the detection threshold θ (horizontal dashed line) at least once within the allowed time window $t \in (0, T)$ (vertical dashed dotted lines), where $t = 0$ indicates the time at which the detector is switched on. If the threshold is crossed at least once in the presence of the signal, then a *correct detection* event for that trial is registered (multiple threshold crossings within the same trial do not matter). The trial average conditional on a frozen value of the signal δ defines the *correct-detection rate* $\mathcal{Y}(\theta, \delta, T)$,

$$\mathcal{Y}(\theta, \delta, T) = \left\langle \max_{t \in (0, T)} \{H[x(t) - \theta]\} \right\rangle_\delta, \quad (4)$$

where $H(\cdot)$ indicates the Heaviside step function. When the signal is absent, i.e., if $\delta = 0$, a response of the detector is to be interpreted as a *false positive*. Hence, the *false-positive rate* $\mathcal{X}(\theta, T)$ is defined as

$$\mathcal{X}(\theta, T) = \mathcal{Y}(\theta, 0, T) = \left\langle \max_{t \in (0, T)} \{H[x(t) - \theta]\} \right\rangle_{\delta=0}. \quad (5)$$

In our simple setup, it directly follows from the definitions Eqs. (4) and (5), that false-positive and correct-detection rates for a given threshold only differ in a static shift of the argument, that is,

$$\begin{aligned} \mathcal{X}(\theta, T) &= f_T(\theta) \\ \mathcal{Y}(\theta, \delta, T) &= f_T(\theta - \delta). \end{aligned} \quad (6)$$

Hence, it suffices to calculate one of the detection rates, e.g., the false-positive rate and its dependence on the threshold $f_T(\theta)$. If we can invert the function, then the ROC curve is

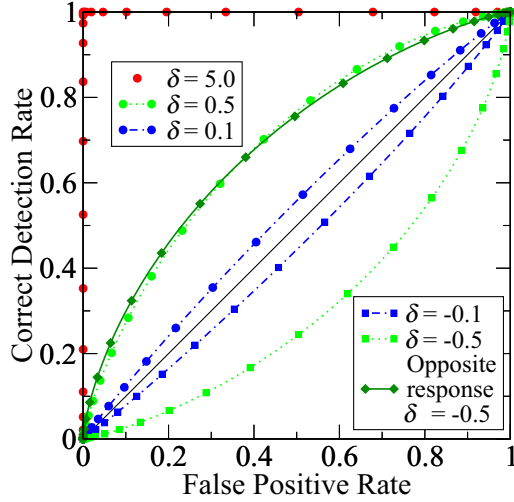


FIG. 2. Receiving operating characteristic (ROC) curves obtained from numerical simulation of Eq. (3) by systematically varying θ for $T = 5$ and different values of δ , as indicated in the legend. Filled circles represent positive values of δ , filled squares refer to negative values, values of δ are distinguished by different line styles (see legend). Dark green diamonds joined by the solid line show are obtained for $\delta = -0.5$ from the detector defined in Eq. (10), which responds in the opposite way as the detector used in the rest of this study.

explicitly given by (see also Refs. [3,10])

$$\mathcal{Y}(\mathcal{X}, \delta, T) = f_T[f_T^{-1}(\mathcal{X}) - \delta]. \quad (7)$$

The ROC curve is obtained by plotting the correct-detection rate as a function of the false-positive rate on systematic variation of the detection threshold θ through all possible values. A few examples of ROC curves for our detector are shown in Fig. 2 for several values of the signal δ , as indicated in the legend. A very high θ corresponds to a very low detector sensitivity and is represented by the lower left corner of the plot range; a low θ corresponds to a high detector sensitivity, which is represented by portion of the ROC curve located in the upper right corner of the plot.

Focusing first on positive values of δ , we can see that for a weak signal ($\delta = 0.1$, blue circles with dash-dotted line in Fig. 2) the ROC curve is close to the diagonal, which represents the chance level, i.e., false-positive and correct-detection rates are equal for any value of θ . When the signal is enhanced ($\delta = 0.5$, green circles with dotted line), the distance of the ROC curve from the diagonal grows. Eventually ($\delta = 5$, red circles with no line), the signal is so large that the ROC curve is close to that of an ideal detector, which can achieve a 100% correct-detection rate with a false-positive rate of 0%.

Turning our attention to the ROC curves obtained at negative values of δ (blue squares with dashed-dotted line and green squares with dotted line for $\delta = -0.1$ and $\delta = -0.5$, respectively), we notice that they are below the chance level, i.e., the detector reacts less often than chance in the presence of a signal. Furthermore, there is a symmetry with respect to the diagonal. In other words, the ROC curve for $-\delta$ is a mirror image of the ROC curve for δ with respect to the line $\mathcal{Y} = \mathcal{X}$. This symmetry makes intuitively sense and can be

better understood by the following simple argument. Defining $\tilde{\theta} = \theta + \delta$ and employing Eq. (6) yields

$$\mathcal{Y}(\theta, -\delta, T) = f_T(\theta + \delta) = \mathcal{X}(\tilde{\theta}, T), \quad (8)$$

$$\mathcal{X}(\theta, T) = f_T(\tilde{\theta} - \delta) = \mathcal{Y}(\tilde{\theta}, \delta, T), \quad (9)$$

which is precisely the symmetry with respect to the diagonal observed in Fig. 2.

Performance below the chance line indicates that the detector defined in Eqs. (4) and (5) is a bad detector in the case $\delta < 0$. Note that if we do not consider the detection procedure as given, and ROC curves are defined as the upper boundary of the ROC space for all feasible tests [5], then no curve below the diagonal line can be an actual ROC curve. One simple way to solve this problem would be to define a new detector, which reacts in the opposite way to Eqs. (4) and (5). The false-positive and correct-detection rates measured by such a detector are

$$\bar{\mathcal{X}}(\theta, T) = 1 - \mathcal{X}(\theta, T), \quad \bar{\mathcal{Y}}(\theta, \delta, T) = 1 - \mathcal{Y}(\theta, \delta, T), \quad (10)$$

respectively. The ROC curve obtained from this reversed procedure for $\delta = -0.5$ is shown in Fig. 2 (dark green diamonds with solid line); it is above chance level and similar, but not exactly the same, as that obtained for $\delta = 0.5$ from the original detection procedure. Rewriting the above equations as $\bar{\mathcal{X}}(\theta, T) - 1/2 = 1/2 - \mathcal{X}(\theta, T)$ and $\bar{\mathcal{Y}}(\theta, \delta, T) - 1/2 = 1/2 - \mathcal{Y}(\theta, \delta, T)$ reveals that the curve is symmetrical with respect to the center point $(1/2, 1/2)$ to that obtained from the original detector (and *not* mirrored around the diagonal like the ROC curves for δ values of opposite sign but from the same detector). In the rest of this study, we will restrict ourselves to positive signals ($\delta > 0$).

As explained in the next subsection, an exact integral expression for $f_T(\theta)$ can be found. Because, however, the numerical quadrature of the integrals proves difficult, in the following subsections we will discuss analytical approximations to the ROC curve as well.

III. RESULTS

A. First-passage-time theory

As outlined above, it suffices to study the probability of a detection in the absence of the signal ($\delta = 0$). In this case, the transition probability density $P(x, t|x_0, t_0)$ corresponding to Eq. (2), i.e., the probability density that the process is around x at time t if it was at x_0 at the earlier time $t_0 < t$, is governed by the well-known Fokker-Planck equation (FPE) [39,40],

$$\partial_t P(x, t|x_0, t_0) = \partial_x(x + \partial_x)P(x, t|x_0, t_0) \quad (11)$$

$$= -\partial_x J(x, t|x_0, t_0), \quad (12)$$

where in Eq. (12) the (conditional) probability current $J(x, t|x_0, t_0)$ was introduced, reflecting the fact that the FPE is a continuity equation.

If we impose natural boundary conditions (relevant for times $t < 0$ prior to the detection window) and wait long enough (or, equivalently, shift the initial time t_0 into the distant past), then the transition probability approaches the stationary

solution

$$P_0(x) = \lim_{t_0 \rightarrow -\infty} P(x, t|x_0, t_0) = \frac{\exp(-x^2/2)}{\sqrt{2\pi}}, \quad (13)$$

a normal distribution with zero mean and unit variance. This is the kind of distribution that is found when the observation time window starts at $t = 0$.

A particular realization can trigger a detection in two ways: (i) the process is above the threshold already at the beginning of the detection window, i.e., $x(0) = x_0 > \theta$; (ii) otherwise, if $x(0) = x_0 < \theta$, $x(t)$ reaches the threshold at least once before $t = T$. In other words, in the second case the first-passage time (FPT) from $x_0 < \theta$ to θ is smaller than T . The probabilities for these two mutually exclusive ways of triggering a detection, p_{inst} and p_{FP} , can be both expressed by integrals and their sum yields the function $f_T(\theta)$,

$$\mathcal{X}(\theta, T) = f_T(\theta) = p_{\text{inst}}(\theta) + p_{\text{FP}}(\theta, T). \quad (14)$$

The first term, the nonvanishing probability $p_{\text{inst}}(\theta)$ to find the process at time $t = 0$ above threshold, is simply given by the integral of the upper tail of the stationary distribution

$$p_{\text{inst}}(\theta) = \int_{\theta}^{+\infty} dx_0 P_0(x_0) = \frac{1}{2} \operatorname{erfc}\left(\frac{\theta}{\sqrt{2}}\right), \quad (15)$$

which in the last step was expressed by the complementary error function [42].

The second term in Eq. (14), i.e., the probability of reaching the threshold before the detector is switched off, is given by the integral of the FPT density from $t = 0$ to $t = T$, i.e., the cumulative FPT probability, averaged over all possible starting positions $x_0 < \theta$:

$$p_{\text{FP}}(\theta, T) = \int_{-\infty}^{\theta} dx_0 P_0(x_0) \int_0^T dt \rho_{\text{FPT}}(t, \theta|x_0). \quad (16)$$

In Eq. (16), $\rho_{\text{FPT}}(t, \theta|x_0)$ is the first-passage time density, i.e., the probability density corresponding to $x(t) = \theta$ given that $x(t = 0) = x_0$. This probability is given by the time-dependent probability current through $x = \theta$, corresponding to the solution of Eq. (11) with an absorbing boundary condition imposed on the threshold, i.e., $P(\theta, t) = 0$ for $t > 0$, and the initial condition $P(x, 0) = \delta(x - x_0)$. Unfortunately, this density cannot be found analytically for a generic initial point $x_0 < \theta$ [43,44]; efficient numerical procedures have been worked out for this problem [45,46], which we will not pursue here. Instead, we will use the fact that, although $\rho_{\text{FPT}}(t, \theta|x_0)$ is not known, its one-sided Fourier transform can be calculated [44,47,48]

$$\hat{\rho}_{\text{FPT}}(\omega, \theta|x_0) = e^{\frac{x_0^2 - \theta^2}{4}} \frac{\mathcal{D}_{i\omega}(-x_0)}{\mathcal{D}_{i\omega}(-\theta)}, \quad (17)$$

where $\mathcal{D}_{i\omega}(z)$ is the parabolic cylinder function [42].

Equation (16) can be rewritten by first substituting

$$\rho_{\text{FPT}}(t, \theta|x_0) = \int_{-\infty}^{+\infty} \frac{d\omega}{2\pi} \hat{\rho}_{\text{FPT}}(\omega, \theta|x_0) e^{-i\omega t} \quad (18)$$

and then performing the time integral from 0 to T :

$$\int_0^T dt \rho_{\text{FPT}}(t, \theta|x_0) = \int_{-\infty}^{+\infty} \frac{d\omega}{2\pi} \frac{1 - e^{-i\omega T}}{i\omega} \hat{\rho}_{\text{FPT}}(\omega, \theta|x_0). \quad (19)$$

The false-positive rate is then

$$\begin{aligned} \mathcal{X}(\theta, T) &= \frac{1}{2} \operatorname{erfc}\left(\frac{\theta}{\sqrt{2}}\right) + \int_0^{+\infty} \frac{d\omega}{\pi} \\ &\times \int_{-\infty}^{\theta} dx_0 P_0(x_0) \operatorname{Re} \left[\frac{1 - e^{-i\omega T}}{i\omega} \hat{\rho}_{\text{FPT}}(\omega, \theta|x_0) \right], \end{aligned} \quad (20)$$

where $\operatorname{Re}[\cdot]$ indicates the real part. Furthermore, we changed the order of integration, and used the Hermitian symmetry of the Fourier-transformed FPT density [$\rho^*(\omega) = \rho(-\omega)$] to restrict the integration with respect to the frequency to the positive range $\omega \geq 0$.

Although Eq. (20) is an exact expression, its practical use is limited by the difficult numerical evaluation of the double integral; see Appendix A. In Sec. III D we will compare Eq. (20) to simulations and the other analytical expressions introduced in the following sections for one specific choice of parameters.

In the next subsection, we discuss an analytical approximation to the ROC curve which is rather simple and surprisingly accurate for most parameter choices.

B. Sampling approximation

The false-positive and correct-detection rates are defined as the probability that $x(t)$ is found at least once above the barrier θ within the allowed time window. One simple approximation of this situation is to replace the Gaussian stochastic process $x(t)$ with a suitable number of discrete draws of a Gaussian *variable*. If these draws are separated by a sufficiently long time interval, then they can be regarded as independent. One reasonable choice is to set this interval equal to the autocorrelation time τ_c of the process [23,49], which is unity in rescaled time units. If these assumptions are made, then the false-positive rate is simply (the index ‘‘sa’’ stands for sampling approximation)

$$\mathcal{X}(\theta, T) \approx \mathcal{X}_{\text{sa}}(\theta, T) = 1 - [p_0(\theta)]^{n(T)}, \quad (21)$$

where

$$\begin{aligned} p_0(\theta) &= 1 - p_{\text{inst}}(\theta) \\ &= \int_{-\infty}^{\theta} dx_0 P_0(x_0) = \frac{1}{2} \left[1 + \operatorname{erf}\left(\frac{\theta}{\sqrt{2}}\right) \right] \end{aligned} \quad (22)$$

is the probability of *not* being above threshold at any given time, and

$$n(T) = T + e^{-T} \quad (23)$$

represents the effective number of draws (in the following the dependence on T will be dropped). While the term T in the above expression should be sufficiently justified by what was said before, the exponential function was chosen arbitrarily as a rapidly decaying function starting at one, which ensures that even for a very short time window the number of effective draws is one, because $\lim_{T \rightarrow 0} n(T) = 1$. Note, furthermore, that n does not need to be an integer and that $n \approx T$ for large time windows.

According to the general relation between false-positive and correct-detection rates expressed by Eq. (6), the correct-

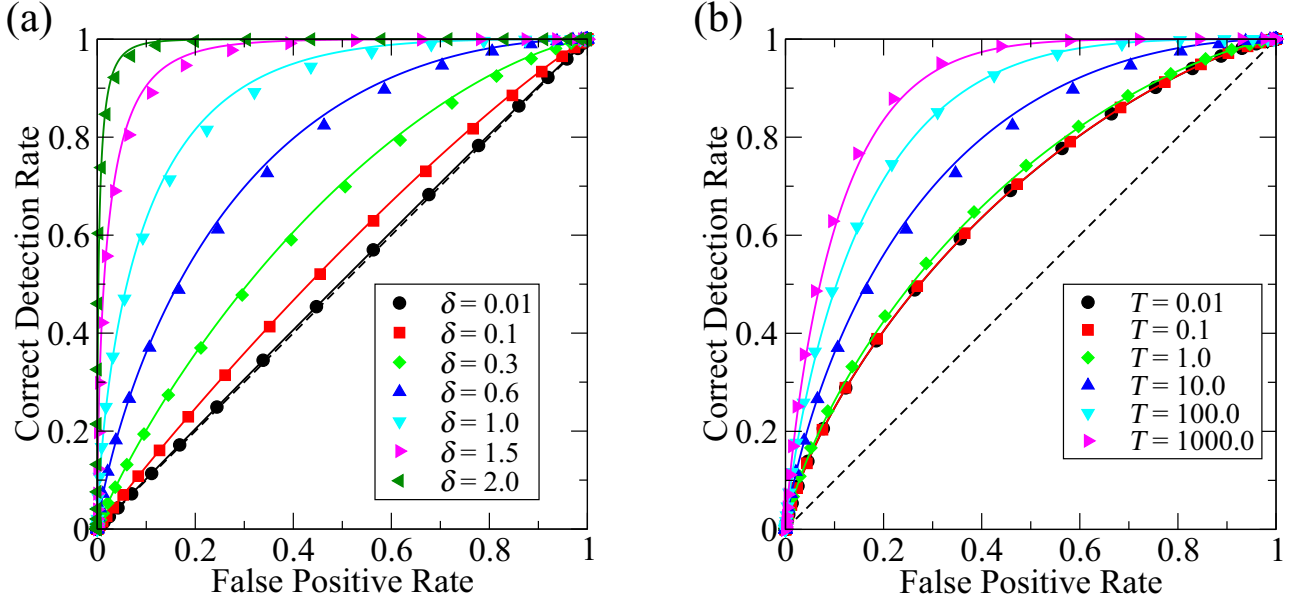


FIG. 3. ROC curves for different values of δ (a) and T (b) obtained from simulations (symbols) together with the sampling approximation Eq. (25) (continuous lines). Parameters: (a) $T = 10$ and (b) $\delta = 0.6$.

detection rate is

$$\mathcal{Y}(\theta, \delta, T) \approx \mathcal{Y}_{\text{sa}}(\theta, \delta, T) = 1 - [p_0(\theta - \delta)]^n. \quad (24)$$

If Eq. (21) is solved for θ and is inserted into Eq. (24), then we obtain

$$\mathcal{Y}_{\text{sa}}(\mathcal{X}, \delta, T) = 1 - \left(\frac{1}{2} \left\{ 1 + \operatorname{erf} \left[\frac{\theta_n(\mathcal{X}_{\text{sa}}) - \delta}{\sqrt{2}} \right] \right\} \right)^n, \quad (25)$$

where

$$\theta_n(\mathcal{X}_{\text{sa}}) = \sqrt{2} \operatorname{erf}^{-1} [2(1 - \mathcal{X}_{\text{sa}})^{\frac{1}{n}} - 1]. \quad (26)$$

For $n = 1$, this formula reduces to the known result for a Gaussian variable with additive signal [6].

Despite the crudeness of the underlying approximation, Eq. (25) is in rather good agreement with the numerical simulations, as shown in Fig. 3. More precisely, Fig. 3(a) shows ROC curves for a fixed time window $T = 10$ and different values of the signal δ . Numerical simulations are indicated by symbols of different shape and color, which correspond to different values of δ , as indicated in the legend. Continuous lines represent the analytical approximation Eq. (25).

When the signal is weak, the ROC curve is close to the diagonal. When the signal is increased, it rapidly approaches the ideal ROC curve. Letting $\delta \rightarrow \infty$ results in $\mathcal{Y}(\mathcal{X}) \rightarrow 1$ for any value of the false-positive rate \mathcal{X} , as is intuitively expected and also confirmed by closer inspection of Eq. (25). Interestingly, the slope of the ROC curve at the origin is always vertical when $\delta > 0$, as shown in Appendix B.

The effect of varying the detection time window T on constant δ is shown in Fig. 3(b), in which the different values of T are represented by different symbols (as indicated in the legend), and the sampling approximation Eq. (25) is represented by solid lines, which agree with simulations rather well. When the detection time window is very short [Fig. 3(b) black circles], the time-dependent process can be well approximated by a single value and the ROC curve is

essentially that of a Gaussian random variable. If the time window is enlarged, then the ROC curve does not change appreciably at first, that is, as long as the time window is shorter than the autocorrelation time of $x(t)$, as a comparison of the ROC curves for $T = 0.01, 0.1, 1$ reveals [black circles, red squares, and green diamonds in Fig. 3(b), respectively]. Further extending the detection time window results in an appreciable increase in the distance of the ROC curve from the diagonal [Fig. 3(b) triangles with different orientations, as indicated in the legend]. Note that each tenfold increment in the time window T causes an increase in the distance of the ROC curve from the diagonal which is maybe twofold at first, and then even smaller. In other words, the growth is rather slow, if compared to the effect of increasing δ .

Although it is clear that $\mathcal{Y}(\mathcal{X}, T)$ can only increase when the detection time window T is enlarged, it is an interesting question whether this growth always saturates at unity or at some other value smaller than one. Because of the very slow growth of \mathcal{Y} as a function of T , exploring this problem numerically beyond the time windows considered in Fig. 3(b) is impractical. In Appendix C, we show by analytical arguments that

$$\lim_{T \rightarrow \infty} \mathcal{Y}_{\text{sa}}(\mathcal{X}, T) = 1 \quad (27)$$

for every nontrivial value of \mathcal{X} (i.e., $\mathcal{X} \neq 0, 1$).

Figure 3 shows that the sampling approximation Eq. (25) is in good agreement with the numerical simulations for many combinations of signal strength and detection time window. In the following, we perform a two-dimensional parameter scan to assess the quality of the approximation in a systematic way. To this end, we introduce the integrated distance between theory and the simulation

$$\varepsilon(\delta, T) = \int_0^1 d\mathcal{X} |\mathcal{Y}_{\text{sa}}(\mathcal{X}, \delta, T) - \mathcal{Y}_{\text{sim}}(\mathcal{X}, \delta, T)|, \quad (28)$$

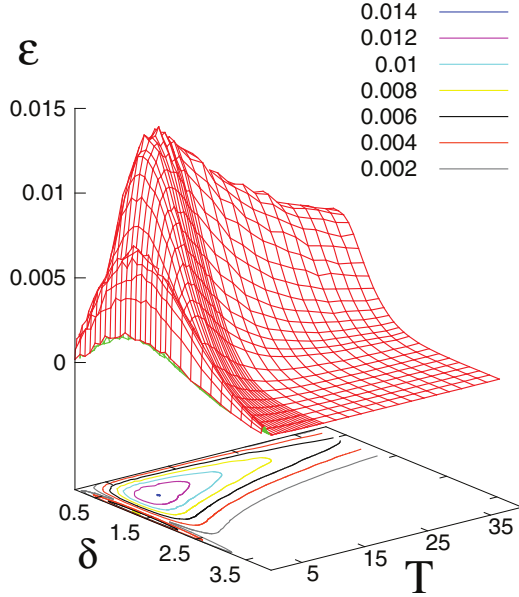


FIG. 4. Integrated absolute deviation between numerical simulations and sampling approximation defined as in Eq. (28) as a function of δ and T .

where $\mathcal{Y}_{\text{sim}}(\mathcal{X}, \delta, T)$ is the correct-detection rate measured in numerical simulations. The results are shown in Fig. 4, which reveals that the discrepancy is largest in the intermediate range of both δ and T , but its absolute magnitude is rather small everywhere. Assuming that for $\delta > 0$, both curves will be above the diagonal and the maximum possible error is $\varepsilon_{\text{max}} = 0.5$; the global maximum in Fig. 4 is less than 3% of this value.

In Sec. III D, we will compare all theoretical approaches considered in this study to each other and to numerical simulations for the choice of parameters ($\delta = 1, T = 5$), which, as seen in Fig. 4, is in the vicinity of the global maximum of the discrepancy ε .

C. High-threshold (Stratonovich) approximation

In the case that the detection threshold is far from the region of high probability, Stratonovich calculated the mean repetition rate of clusters of threshold crossings [41], which is

$$\lambda_0(\theta) = \left(\sqrt{2\pi} \int_0^\theta dx e^{-\frac{x^2}{2}} \right)^{-1}. \quad (29)$$

When the threshold is high, the probability that $x(t)$ is found above threshold in the absence or presence of the signal is low and can be approximated by the crossing rate times the time window

$$\mathcal{X}(\theta, T) \approx \mathcal{X}_{\text{str}}(\theta, T) = \lambda_0(\theta)T = \frac{iT/\pi}{\text{erf}[i(\theta)/\sqrt{2}]} \quad (30)$$

$$\begin{aligned} \mathcal{Y}(\theta, \delta, T) &\approx \mathcal{Y}_{\text{str}}(\theta, \delta, T) = \lambda_0(\theta - \delta)T \\ &= \frac{iT/\pi}{\text{erf}[i(\theta - \delta)/\sqrt{2}]}, \end{aligned} \quad (31)$$

where the integral in Eq. (29) was replaced by using the error function with imaginary argument.

Equation (29) was derived by Stratonovich as the inverse mean FPT of the level θ starting from zero, under the assumption that θ is high [41]. He also pointed out that the choice of the starting level (here the origin) is not crucial as long as it lies within the region of high probability. Assuming that $x(t)$ starts in the region of high probability, however, implies that the possibility that $x(t = 0)$ is already above the threshold is discarded. Hence, the approximation is not valid in the limit of very small detection time window $T \rightarrow 0$. This limit case could be easily accounted for by adding the corresponding probabilities p_{inst} from Eq. (15) to the above estimates of \mathcal{X} and \mathcal{Y} .

In the following subsection, we compare all theoretical expressions introduced above to numerical simulations and show in particular that Eqs. (30) and (31) are accurate when the threshold is high and the detection rate is small, as expected.

D. Comparison of the different analytical expressions

The various results from our exact expression, simulations, and approximations are compared in Fig. 5 for a parameter set for which the sampling approximation shows a pronounced deviation from simulation results ($\delta = 1, T = 5$, close to the global maximum of the deviation shown in Fig. 4); the ROC curve is plotted in Fig. 5(a), while false-positive and correct-detection rates are shown in Figs. 5(b) and 5(c).

As we can expect, the first-passage-time theory (represented by dashed lines) shows in all panels an excellent agreement with the simulation results (its numerical evaluation, however, may take longer than the Langevin simulations). We also observe that the false-positive and correct-detection rates obtained from the sampling approximation Eqs. (24) and (21) differ rather strongly by a constant shift from the simulation data when they are considered separately, as shown in Fig. 5(b) (solid lines). Such a rigid shift, however, does not alter much the correctness of the ROC curve, as long as the shape of the false-positive rate $\mathcal{X}_{\text{sa}}(\theta, T)$ is similar to the actual $f_T(\theta)$. To understand why, we first recall that

$$\mathcal{X}(\theta, T) = f_T(\theta), \quad (32)$$

$$\mathcal{Y}(\theta, \delta, T) = f_T(\theta - \delta), \quad (33)$$

$$\mathcal{Y}(\mathcal{X}, \delta, T) = f_T(f_T^{-1}(\mathcal{X}) - \delta), \quad (34)$$

and notice that any constant shift applied to the argument of $f_T(\theta)$ in Eqs. (32) and (33) cancels out in the ROC curve Eq. (34). This fact is visualized in Fig. 5(c), in which the correct-detection and false-positive rate from the sampling approximation (solid lines) are shifted by the same amount. It can be seen that the two curves fit the simulation results almost as well as the exact FPT theory, which explains why, despite the discrepancy observed in the prediction of correct-detection and false-positive rates separately, the sampling approximation yields a rather good prediction of the ROC curve.

It is not surprising that the sampling approximation underestimates the actual $f_T(\theta)$, because it completely neglects all threshold crossings that occur between consecutive samples. In Appendix D, we present a way to improve the sampling approximation in this respect. Briefly, we perform a linearization

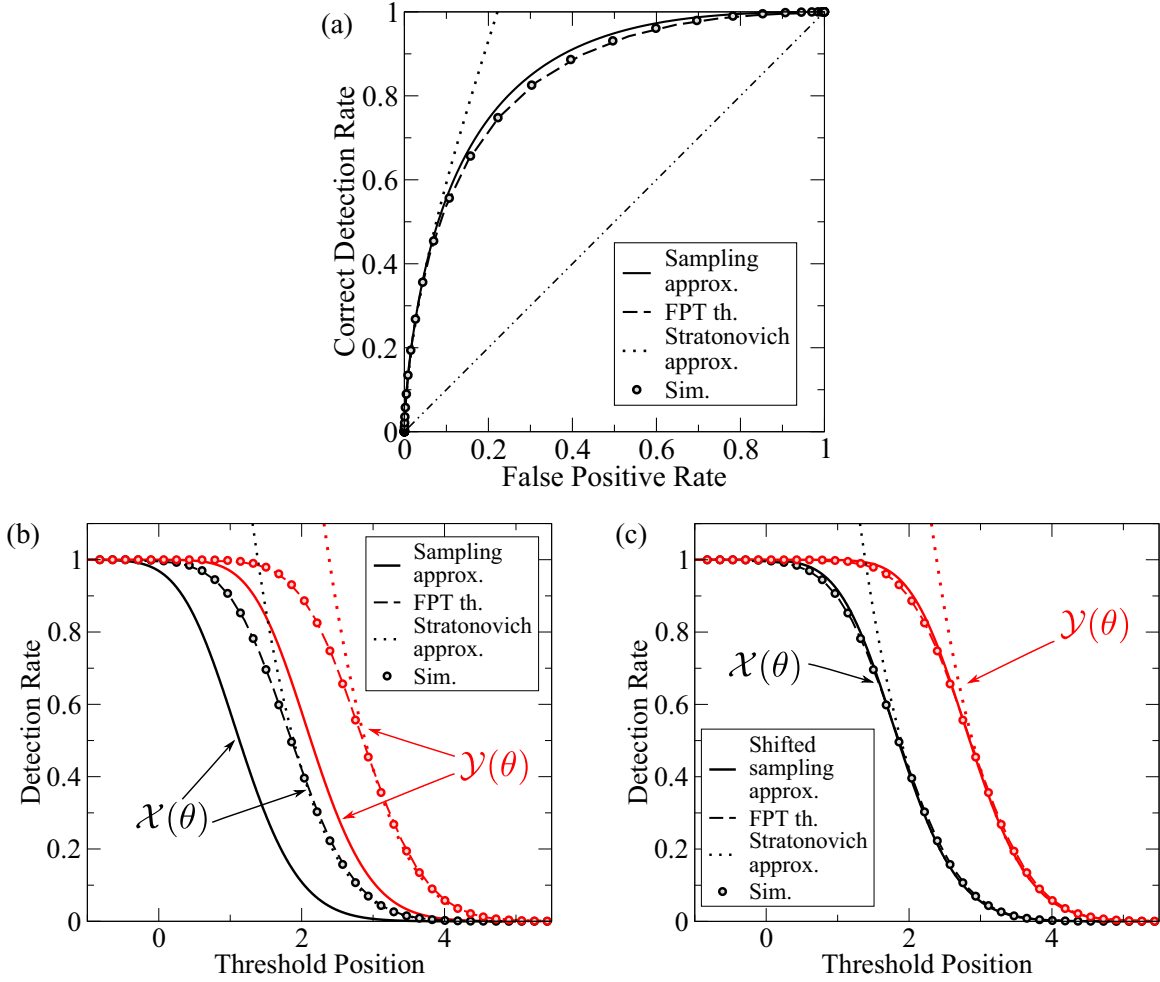


FIG. 5. Comparison of the three theoretical approaches pursued here, the sampling approximation (continuous line), the FPT theory (dashed line), and the Stratonovich approximation (dotted line), to numerical simulations (filled circles). (a) ROC curve; (b) correct-detection rate \mathcal{Y} and false-positive rate \mathcal{X} as a function of the threshold θ ; (c) same as panel (b), but with a rigid shift along the θ axis in the sampling approximation (same shift for \mathcal{X}_{sa} , \mathcal{Y}_{sa} , chosen such that the approximations agree with the exact FPT theory when they attain the value 1/2). See Appendix D for a way to improve the sampling approximation and a discussion of the causes underlying the discrepancy between the sampling approximation and the actual $f_T(\theta)$. Parameters: $\delta = 1.0$ and $T = 5$; for this choice the discrepancy between sampling approximation and simulations is close to the global maximum (see Fig. 4).

of the parabolic potential near the threshold and account for trajectories that cross the threshold within a time window of unit length, i.e., within one correlation time from the last sample. The analysis of this improved sampling approximation also provides a plausible reason for why the regular sampling approximation well approximates the shape of $f_T(\theta)$, as seen in Figs. 5(b) and 5(c) and discussed above.

Last, we note that the Stratonovich approximation (dotted line) gives us a reliable *absolute* estimate for \mathcal{X} and \mathcal{Y} for high thresholds [Figs. 5(b) and 5(c)]. Accordingly, the shape of the ROC curve in the lower left corner of Fig. 5(a) is also accurately predicted. However, for false-positive rates larger than $\mathcal{X} \gtrsim 0.1$ the discrepancy is large. We would like to add here that a qualitative approximation for the full range can be found by using a Poisson-like approximation for the false-positive rate $\mathcal{X}_{str,2}(\theta, T) = 1 - \exp[-\lambda_0(\theta)T]$, with $\lambda_0(\theta)$ as given in Eq. (29). Doing this constrains the range of values to $[0,1]$ as expected for a probability, and the resulting shape

of $f_T(\theta)$ is roughly similar to that measured in simulations. However, the resulting ROC curve is significantly worse than that obtained from the sampling approximation and is therefore neither shown nor further discussed here.

E. Outlook: Low-pass filtered noise and multiplicative signal

In the previous subsection we briefly argued (see Appendix D for a more detailed discussion) that missed crossings between samples are the major cause for the underestimation of the detection rates seen in the sampling approximation. If this is the case, then we expect the discrepancy to be smaller if smoother stochastic processes are considered. To give some support to this hypothesis, we test here how the sampling approximation performs for a low-pass filtered OU process. In other words, we replace the driving white Gaussian noise in Eq. (1) with an OU process $\eta(t)$ with exponential correlation

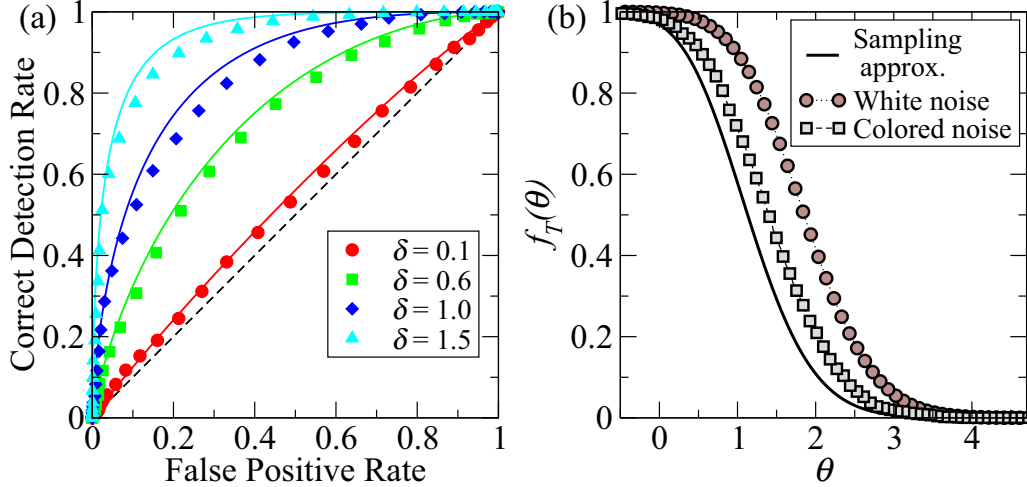


FIG. 6. (a) Receiver operating characteristic curves obtained for low-pass filtered OU process, Eqs. (35) and (36). Filled symbols are numerical simulations corresponding to different values of δ , as indicated in the legend; solid lines represent the sampling approximation. (b) Comparison of the detection rate $f_T(\theta)$ obtained from the sampling approximation (black solid line) to numerical simulations of the unfiltered OU process, i.e., driven by white noise (filled circles), and to numerical simulations of the low-pass filtered OU process, i.e., driven by colored noise (filled squares). Parameters: $T = 5$, $\Delta t = 10^{-4}$, and $N_{\text{trials}} = 2 \times 10^6$.

function $C_{\eta\eta}(t) = \sigma_\eta^2 e^{-|t|/\tau}$ generated by a second stochastic differential equation:

$$\tau \dot{x}(t) = -x(t) + \delta + \eta(t), \quad (35)$$

$$\tau \dot{\eta}(t) = -\eta(t) + \sqrt{2\sigma_\eta^2 \tau} \xi(t). \quad (36)$$

The autocorrelation function of $x(t)$ is

$$C_{xx}(t) = \sigma_\eta^2 \frac{1 + |t|/\tau}{2} e^{-|t|/\tau}. \quad (37)$$

Hence, the variance of x is $\sigma_x^2 = \sigma_\eta^2/2$, and its autocorrelation time is

$$\tau_c = \int_0^\infty dt \frac{C_{xx}(t)}{C_{xx}(0)} = \int_0^\infty dt (|t| + \tau) \frac{e^{-|t|/\tau}}{\tau} = 2\tau. \quad (38)$$

Numerical simulation of Eqs. (35) and (36) is done with an Euler procedure analogous to Eq. (3). Initial conditions for x, η are drawn from a bivariate Gaussian distribution with correlation coefficient $\rho = C_{x\eta}(0)/\sqrt{C_{\eta\eta}(0)C_{xx}(0)} = 1/\sqrt{2}$, where $C_{x\eta}(0)$ is the cross-correlation at zero lag. The detection procedure is the same as in the rest of this study (see Sec. II).

If we set $\tau = 1/2$ and $\sigma_\eta^2 = 2$ in Eqs. (35) and (36), then $x(t)$ has unit variance, and its autocorrelation time is $\tau_c = 1$. With this choice, variance and autocorrelation time of $x(t)$ are equal to one, so that the sampling approximation can be applied as in Eqs. (21) and (24) with no modifications.

Figure 6(a) shows the ROC curves obtained from numerical simulations for several values of δ (filled symbols as indicated in the legend). The continuous lines in the corresponding color represent the sampling approximation, which is in good agreement with the simulations. Furthermore, Fig. 6(b) shows that the underestimation of the detection rate $f_T(\theta)$ is much less severe for the case of colored noise than for the case of white noise [same data as in Fig. 5(b)], which supports the initial supposition about the reasons of the discrepancy seen in the sampling approximation.

As a final possible extension of the basic problem, we consider the situation in which signal is still static, but not additive. Instead, it affects the noise intensity, as it happens in many cases of interest [50–55]. Going back to the basic definition of our system with units Eq. (1), we consider a signal $\beta > 0$ that modulates the noise intensity (we set the additive signal to zero for simplicity)

$$\tau_c \dot{\hat{x}}(t) = -\hat{x}(t) + \sqrt{2(1 + \beta)\sigma_x^2 \tau_c} \xi(t). \quad (39)$$

Once again, we compute the ROC curve for a given strength of the signal β .

If we rescale time in units of τ_c and measure the displacement \hat{x} in units of $\sigma_{\hat{x}}$, as done in Sec. II, then Eq. (39) becomes

$$\dot{x}(t) = -x(t) + \sqrt{2(1 + \beta)} \xi(t). \quad (40)$$

Correct-detection and false-positive events will be registered, as above, when the process exceeds the threshold θ at least once within the detection window T . Hence, correct-detection and false-positive rates are defined as in Eqs. (5) and (4) with β playing the role of δ .

When $\beta = 0$, Eq. (40) is identical to Eq. (2) with $\delta = 0$. Indeed, in the absence of any signals there is no difference to the situation considered in the previous sections. Therefore, the false-positive rate will not change in this new scenario and be equal to

$$\mathcal{X}_{\text{ms}}(\theta, T) = f_T(\theta), \quad (41)$$

where $f_T(\theta)$ is the same function as in the previous case, as in Eq. (6).

Dividing by $\sqrt{1 + \beta}$ casts Eq. (40) into an equation that is, once more, formally equivalent to the case of no signal:

$$\dot{\hat{x}}(t) = -\hat{x}(t) + \sqrt{2} \xi(t), \quad (42)$$

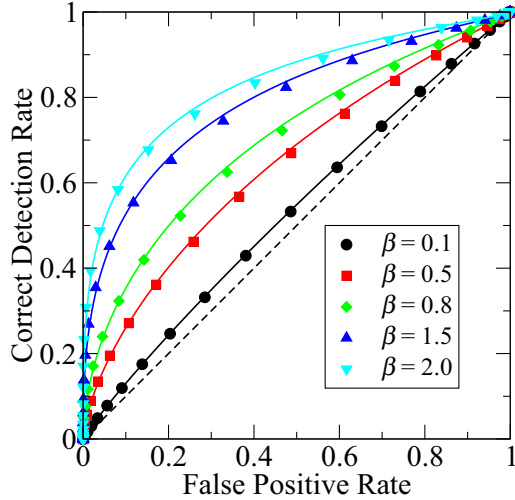


FIG. 7. Examples of ROC curves obtained for a static modulation of the noise intensity, as in Eq. (40), for different values of β with $T = 5$. Continuous lines are obtained from Eqs. (41) and (43), where $f_T(\theta) = \mathcal{X}_{sa}(\theta, T)$, i.e., the sampling approximation Eq. (21).

where $\bar{x} = x/\sqrt{1+\beta}$. This rescaling, however, involves the threshold as well, which changes to $\bar{\theta} = \theta/\sqrt{1+\beta}$. Hence, the correct-detection rate is equal to the false-positive rate with rescaled threshold

$$\mathcal{Y}_{ms}(\beta, \theta, T) = \mathcal{X}_{ms}(\bar{\theta}, T) = f_T\left(\frac{\theta}{\sqrt{1+\beta}}\right). \quad (43)$$

Note that this is a general argument and does not depend on how $f_T(\theta)$ is computed or estimated. As an example of these ideas, Fig. 7 shows the ROC curves obtained from numerical simulations for several values of the signal β , as indicated in the legend, together with theoretical estimates obtained from the sampling approximation combined with Eqs. 41) and (43). Interestingly, Fig. 7 shows that the shape of the ROC curves is less symmetrical than that for an additive signal [Fig. 3(a)], and the agreement between the theory and simulations is rather good for all tested values of β .

IV. DISCUSSION

In this study, we considered a static signal embedded in an Ornstein-Uhlenbeck noise. The assumption of a *static* signal is meant to be an idealized representation of a broader situation, i.e., a signal affected by noise which is temporally correlated on timescales that are much faster than those of the signal. In this sense, we investigated the problem in a controlled environment, in which it was possible to perform extensive numerical simulations and to work out an exact expression against which we could test ideas that can be applied in other contexts. In fact, the basic idea underlying the sampling approximation was already explored to deal with a specific detection problem involving a nonstatic signal [23,24,49,56], and this approximation worked satisfactorily in this more general situation as well.

In the present study, the response of the detector was triggered whenever the process exceeded a fixed threshold within the allowed time. The simplicity of this mechanisms

makes it also very general. Indeed, threshold systems with external drive are used to model extremely diverse phenomena, which encompass earthquakes [18,57], credit defaults in bond markets [58,59], the firing threshold in neuronal models [60], tipping points in climate models [61], among others. In the context of signal detection and processing, noise in threshold elements can lead to the remarkable phenomenon of stochastic resonance [62] (SR). In single threshold-based or bistable systems, SR was discovered both for subthreshold [48,63,64] and suprathreshold signals (resonant trapping) [65]; a different mechanism for suprathreshold stochastic resonance (SSR) was revealed in arrays of threshold elements [66,67]. Typically, SR and SSR are quantified by means of the signal-to-noise ratio, or spectral and information-theoretic measures. However, to measure SR in bistable potentials [68–70], ROC curves have also been employed [9,71]. The framework put forward in the present study could be extended to investigate the SSR by using ROC curves, and to explore how a finite detection time window affects SSR (it has been shown, for instance, that a finite time window for encoding has a drastic effect on the signal distribution that maximizes channel capacity [72,73]).

As discussed in Sec. (III D), the sampling approximation misses a lot of crossings, and the detection rates, taken separately, are underestimated by the sampling approximation. A way to account for these missed crossings and improve the approximation is discussed in Appendix D. This improved approximation, however, involves an integral expression that cannot be solved analytically. Although its numerical integration is considerably easier than that of the full FPT theory, the improved sampling approximation is still more cumbersome than the regular sampling approximation and, more importantly, it is not clear whether it can be straightforwardly extended to other stochastic processes, as opposed to the regular sampling approximation, which can be applied as it is to any Gaussian process of known stationary variance and autocorrelation time. In this respect, we note that the Ornstein-Uhlenbeck process is “jagged,” i.e., it is everywhere non-differentiable. Consequently, each time the process reaches a certain level, a cluster of infinitely many crossings occur, as discussed by Stratonovich [41], which suggests that the underestimation of the single detection rates would be less severe for smooth processes. The preliminary results for a low-pass filtered OU process presented in Sec. III E support this conjecture and demonstrate how easily the sampling approximation can be applied to any Gaussian stationary process of known autocorrelation function. Given the simplicity of the underlying idea, it can be expected that some discrepancy between the sampling approximation and the actual $f_T(\theta)$ is unavoidable also for smooth processes. However, we remark that discrepancies in the single detection rates such as those observed in Sec. III D and Fig. 6(b) do not affect important summary statistics (such as the area under the curve) that depend solely on the ROC curve, which was approximated rather well in all considered cases.

We also briefly explored the generalization of a static modulation of the noise intensity of the process, which could be understood as a caricature of an integrator reading out a slow modulation of the variance of the activity of a population [74–76]. In the more general case, a signal will affect all

statistical properties of the process in different ways. While it is unlikely that in such a complex scenario an exact analytical treatment is possible, we remark that the basic idea of the sampling approximation can still be used, as long as the signal varies slowly.

Can the methods presented here be generalized to the case of a time-dependent signal or a time-dependent threshold? First-passage problems with time-dependent parameters are generally much more difficult [77–80]; however, in the limit case of weak time-dependent modifications to the signal or the threshold, results from Refs. [81,82] may be applicable, at least if the underlying noise process is simple.

ACKNOWLEDGMENTS

We acknowledge useful preliminary explorations of this study's subject with Günther Waldner [83]. This work was supported by the German Research Foundation (DFG) Grant No. GRK 1589/2.

APPENDIX A: NUMERICAL INTEGRATION OF EQ. (14)

The numerical evaluation of the double integral in Eq. (14) is nontrivial and for the full range of thresholds rather difficult. For the parameter set discussed in Sec. III D and the results displayed in Fig. 5, we have evaluated the double integral as follows. For the integration with respect to x_0 we replaced the range $(-\infty, \theta)$ by $(x_{\text{-inf}}, \theta)$ with $x_{\text{-inf}} = -5$ and tested for selected values of the threshold that the result did not change on enlarging the interval. Concerning the integration with respect to ω , for the frequency interval $\omega \in (0, 10)$ we used the full expression for the parabolic cylinder functions in Eq. (18), for the range $(10, \omega_{\text{max}})$ we used the high-frequency approximation for the parabolic cylinder functions [48,84]

$$\begin{aligned} \mathcal{D}_a(z) &\sim \frac{1}{\sqrt{2}} \exp \left\{ iz\sqrt{a} + \frac{a}{2} [\ln(a/e) - i\pi] \right\} \\ &\quad \times \sum_{n=0}^2 i^n (2a)^{-n/2} Q_n(z) \\ Q_0(z) &= 1, \quad Q_1(z) = -\frac{z(z^2 - 6)}{12\sqrt{2}}, \\ Q_2(z) &= \frac{z^6 - 12z^4 - 36z^2 + 96}{576}. \end{aligned} \quad (\text{A1})$$

The integration over x_0 can be carried out analytically in this approximation (but not if the exact parabolic cylinder functions are used). For the integration with respect to frequency, we used a numerical integration of *xmapple*, the NAG routine *d01akc*, which employs adaptive Gauss 30-point and Kronrod 61-point rules.

The upper limit ω_{max} turned out to be particularly critical for low values of the threshold. For instance, for $\theta = 0.25$ and lower, we needed at least $\omega = 10^4$ to obtain convergence within the line thickness of Fig. 5.

APPENDIX B: SLOPE OF THE ROC CURVE IN THE LIMIT $\mathcal{X} \rightarrow 0$

We consider the slope of the ROC curve as $\mathcal{X} \rightarrow 0$ as computed from the sampling approximation Eq. (25), i.e., the limit

$$\lim_{\mathcal{X}_{\text{sa}} \rightarrow 0} \frac{d\mathcal{Y}_{\text{sa}}(\mathcal{X}_{\text{sa}})}{d\mathcal{X}_{\text{sa}}} = \lim_{\theta \rightarrow +\infty} \frac{d\mathcal{Y}_{\text{sa}}}{d\theta} \frac{d\theta}{d\mathcal{X}_{\text{sa}}} = \lim_{\theta \rightarrow +\infty} \frac{\frac{d\mathcal{Y}_{\text{sa}}}{d\theta}}{\frac{d\mathcal{X}_{\text{sa}}}{d\theta}}, \quad (\text{B1})$$

where the change of variable in the second step was done according to Eq. (26). Intuitively, a low false-positive rate is equivalent to increasing the threshold. It follows from Eq. (24) that

$$\frac{d\mathcal{Y}_{\text{sa}}}{d\theta} = n[p_0(\theta - \delta)]^{n-1} \frac{dp_0(\theta - \delta)}{d\theta}, \quad (\text{B2})$$

where the derivative $\frac{dp_0(\theta - \delta)}{d\theta}$ is simply a Gaussian function. In this and in the following section we will make often use of the asymptotic expansion of the error function for large arguments [42]:

$$\text{erf}(x) \approx 1 - \frac{e^{-x^2}}{x\sqrt{\pi}}. \quad (\text{B3})$$

By exploiting Eqs. (B2) and (B3), we can rewrite Eq. (B1) as follows:

$$\begin{aligned} \lim_{\theta \rightarrow +\infty} \frac{\frac{d\mathcal{Y}_{\text{sa}}}{d\theta}}{\frac{d\mathcal{X}_{\text{sa}}}{d\theta}} &= \frac{(1 - e^{-\theta^2/2} e^{\theta\delta - \delta^2/2})^{n-1} e^{\theta\delta - \delta^2/2}}{(1 - e^{-\theta^2/2})^{n-1}} \\ &= \lim_{\theta \rightarrow +\infty} e^{\theta\delta - \delta^2/2}. \end{aligned} \quad (\text{B4})$$

Hence, if $\delta > 0$, then

$$\lim_{\mathcal{X}_{\text{sa}} \rightarrow 0} \frac{d\mathcal{Y}_{\text{sa}}(\mathcal{X}_{\text{sa}})}{d\mathcal{X}_{\text{sa}}} = \lim_{\theta \rightarrow +\infty} \frac{d\mathcal{Y}_{\text{sa}}}{d\theta} \frac{d\theta}{d\mathcal{X}_{\text{sa}}} = +\infty. \quad (\text{B5})$$

In other words, the ROC curves always intersect the point (0,0) vertically except when when $\delta = 0$. In this case, the ROC curve is the diagonal, which has slope one everywhere.

The result in Eq. (B5) can be derived also from the Stratonovich approximation Eq. (31), which is valid exactly in the limit of small false-positive rate. To this end, we use the asymptotic expansion of the error function in Eq. (31), which is in this case equivalent to the expansion of the integral in Eq. (29) (see Ref. [41]),

$$\begin{aligned} \lim_{\mathcal{X}_{\text{str}} \rightarrow 0} \frac{d\mathcal{Y}_{\text{str}}(\mathcal{X}_{\text{str}})}{d\mathcal{X}_{\text{str}}} &= \lim_{\theta \rightarrow +\infty} \frac{\frac{d\mathcal{Y}_{\text{str}}}{d\theta}}{\frac{d\mathcal{X}_{\text{str}}}{d\theta}} \\ &= \lim_{\theta \rightarrow +\infty} \frac{(\theta - \delta)e^{-\theta^2/2} e^{\theta\delta - \delta^2/2}}{\theta e^{-\theta^2/2}} \\ &= \lim_{\theta \rightarrow +\infty} e^{\theta\delta - \delta^2/2} = +\infty, \end{aligned} \quad (\text{B6})$$

which is consistent with Eq. (B5).

APPENDIX C: ASYMPTOTIC LIMIT OF $\mathcal{Y}_{\text{sa}}(\delta, \theta, T)$ FOR $T \rightarrow \infty$

Here, we discuss the limiting behavior of the correct-detection rate $\mathcal{Y}_{\text{sa}}(\mathcal{X}, T)$ for infinitely large detection time window at a fixed false-positive rate. Because $n = T + e^{-T}$, the limit $T \rightarrow \infty$ is equivalent to $n \rightarrow \infty$. Hence, we can

consider Eq. (25) as a function of n (we will also drop the index sa on \mathcal{X} and \mathcal{Y} as well as all arguments other than n to avoid an overladen notation)

$$\mathcal{Y}(n) = 1 - \left\{ \frac{1}{2} \left[1 + \operatorname{erf} \left(\frac{\theta_n}{\sqrt{2}} - \frac{\delta}{\sqrt{2}} \right) \right] \right\}^n, \quad (\text{C1})$$

and recall that

$$\theta_n = \sqrt{2} \operatorname{erf}^{-1} [2(1 - \mathcal{X})^{\frac{1}{n}} - 1] \quad (\text{C2})$$

is the position of the threshold. Although it is a function of both n and \mathcal{X} , \mathcal{X} is fixed, and this dependence is therefore omitted for simplicity. It follows from Eq. (C2) that $\theta_n \rightarrow +\infty$ when $n \rightarrow \infty$. It is also intuitively clear that the threshold must be increased to keep the false-positive rate constant while increasing the detection time window. A simple rearrangement of Eq. (C2) leads to

$$\operatorname{erf} \left(\frac{\theta_n}{\sqrt{2}} \right) = 2e^{\frac{\ln(1-\mathcal{X})}{n}} - 1 \approx 1 + 2 \frac{\ln(1-\mathcal{X})}{n}, \quad (\text{C3})$$

where we replaced the exponential function on the right side by its series expansion up to the linear term. Because θ_n is large, we can replace the error function on the left-hand side of Eq. (C3) with its asymptotic expansion Eq. (B3). Performing this substitution and rearranging yields

$$\frac{e^{-\theta_n^2/2}}{\sqrt{2\pi}\theta_n} \approx -\frac{\ln(1-\mathcal{X})}{n}, \quad (\text{C4})$$

which is valid for large n . Turning back to Eq. (C1), if we replace once again the error function by its asymptotic expansion for large argument Eq. (B3), rearrange, and use Eq. (C4), we obtain

$$\begin{aligned} \lim_{n \rightarrow +\infty} \mathcal{Y}(n) &= \lim_{n \rightarrow +\infty} 1 - \left(1 - \frac{e^{-\frac{\theta_n^2}{2}}}{\sqrt{2\pi}\theta_n} \frac{\theta_n e^{\theta_n \delta - \frac{\delta^2}{2}}}{\theta_n - \delta} \right)^n, \\ &= \lim_{n \rightarrow +\infty} 1 - \left[1 + \frac{\ln(1-\mathcal{X})}{n} \frac{\theta_n e^{\theta_n \delta - \frac{\delta^2}{2}}}{\theta_n - \delta} \right]^n, \\ &= \lim_{n \rightarrow +\infty} 1 - \left[1 + \frac{\ln(1-\mathcal{X})}{n} \alpha(n, \delta) \right]^n, \end{aligned} \quad (\text{C5})$$

where in the last step we defined

$$\alpha(n, \delta) = \frac{\theta_n e^{\theta_n \delta - \frac{\delta^2}{2}}}{\theta_n - \delta} \quad (\text{C6})$$

and we point out that the term $\frac{\ln(1-\mathcal{X})}{n} \alpha(n, \delta) < 0$.

If $\delta > 0$ and n is large, then $\alpha(n, \delta)$ is an increasing function of n that grows without bound, because, recalling Eq. (C2), $\theta_n \rightarrow +\infty$ when $n \rightarrow \infty$. Hence, for every n greater than a (large) fixed value $n \geq \bar{n}$, we find

$$\alpha(n, \delta) \geq \alpha(\bar{n}, \delta) \quad (\text{C7})$$

and

$$\lim_{n \rightarrow +\infty} \mathcal{Y}(n) = \lim_{n \rightarrow +\infty} 1 - \left[1 + \frac{\ln(1-\mathcal{X})}{n} \alpha(n, \delta) \right]^n, \quad (\text{C8})$$

$$\geq \lim_{n \rightarrow +\infty} 1 - \left[1 + \frac{\ln(1-\mathcal{X})}{n} \alpha(\bar{n}, \delta) \right]^n, \quad (\text{C9})$$

$$= 1 - \exp[\ln(1-\mathcal{X})^{\alpha(\bar{n}, \delta)}], \quad (\text{C10})$$

$$= 1 - (1-\mathcal{X})^{\alpha(\bar{n}, \delta)} \xrightarrow{\bar{n} \rightarrow \infty} 1, \quad (\text{C11})$$

where in Eq. (C10) we used the definition of the exponential function, and in Eq. (C11) we made $\alpha(\bar{n}, \delta)$ arbitrarily large by increasing \bar{n} (we assumed $\mathcal{X} \neq 0, 1$ since the beginning). Because $\mathcal{Y}(n) \leq 1$ by definition, we conclude that

$$\lim_{n \rightarrow +\infty} \mathcal{Y}(n) = 1, \quad (\text{C12})$$

and we argue that the slow growth of the correct-detection rate as a function of T observed in Fig. 3 must always converge to 1.

APPENDIX D: REFINEMENT OF SAMPLING APPROXIMATION

In this Appendix, we discuss an improvement of the sampling approximation, which points out the principal reason for the underestimation of detection rates and provides a likely explanation of the fact observed in Fig. 5, that such underestimation can be resolved by a static shift in the argument of the sampling approximation.

The picture underlying the sampling approximation Eq. (21) is that the detection time window can be divided in segments of unit length (provided that time is measured in unit of the autocorrelation time of the process), which can be approximated as independent. In each time interval, the trajectory of the process is replaced by one sample, such that all threshold crossings that can happen between two draws of the process are missed. Hence, the sampling approximation underestimates the actual detection rates.

In order to improve the approximation, we replace the probability to be under the threshold $p_0(\theta)$ by a corrected probability $p_1(\theta)$

$$\mathcal{X}(\theta, T) \approx \mathcal{X}_{\text{rsa}}(\theta, T) = 1 - [p_1(\theta)]^{n(T)}. \quad (\text{D1})$$

Here [in accordance with the first-passage-time theory of Sec. (III A)], $p_1(\theta)$ is the probability that the trajectory is found below θ at the sampling point *and* that it does not cross the threshold until the next sample is drawn:

$$p_1(\theta) = \int_{-\infty}^{\theta} dx_0 \frac{e^{-\frac{x_0^2}{2}}}{\sqrt{2\pi}} \gamma(\theta, x_0), \quad (\text{D2})$$

$$= \int_{-\infty}^{\theta} dx_0 \frac{e^{-\frac{x_0^2}{2}}}{\sqrt{2\pi}} \left[1 - \int_0^1 dt J(t, \theta | x_0) \right]. \quad (\text{D3})$$

In Eq. (D3), $J(t, \theta | x_0)$ indicates the probability flux through the detection threshold θ at time t with absorbing boundary condition at θ and initial condition $x(0) = x_0$. Note that neglecting the trajectories that exceed the threshold is equivalent to setting the term $J(t, \theta | x_0) = 0$. By doing so, $\gamma(\theta, x_0) = 1$ and the original sampling approximation Eq. (21) is recovered.

As discussed in Sec. III A, the true probability flux can be expressed as an integral over parabolic cylinder functions, the numerical evaluation of which is difficult. If, however, the parabolic potential is linearized at the threshold, i.e., if the actual drift term is replaced by the constant value $-\theta$, then

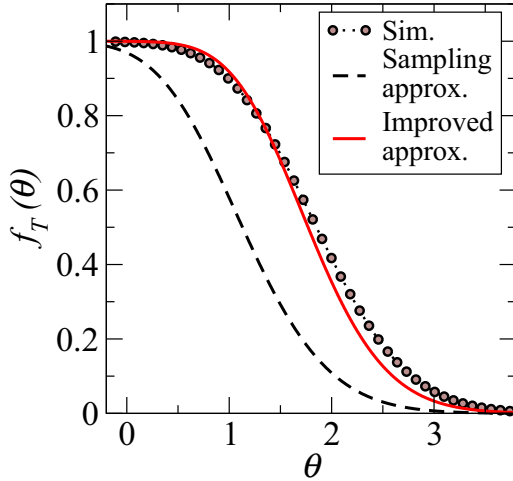


FIG. 8. The improved sampling approximation obtained by combining Eqs. (D1) and (D5) (red solid line) is in better agreement with numerical simulations (filled circles) than the regular sampling approximation Eq. (21) (black dashed line). Parameters are as in Fig. 5.

we obtain a diffusion process with drift, which can be solved, for instance, by constructing the solution with the method of images [85]. The probability flux is then

$$J(t, \theta|x_0) \approx \frac{(\theta - x_0)}{\sqrt{4\pi t^3}} \exp\left[-\frac{(\theta - x_0 + \theta t)^2}{4t}\right]. \quad (\text{D4})$$

Note that when $\theta > 0$, which is the most relevant case, the drift term is directed away from the threshold, and the integral from zero to infinity of Eq. (D4) is smaller than one. In other words, the first-passage-time distribution is defective, reflecting the fact that a finite fraction of trajectories needs

an infinite time to reach the threshold [86], an artifact of the approximation, which tends to underestimate the actual probability flux with the original parabolic potential. Finally, we obtain

$$p_1(\theta) = \frac{1}{2} \left[1 + \operatorname{erf}\left(\frac{\theta}{\sqrt{2}}\right) \right] - \int_{-\infty}^{\theta} dx_0 \int_0^1 dt \frac{e^{-\frac{x_0^2}{2}}}{\sqrt{2\pi}} \frac{(\theta - x_0)}{\sqrt{4\pi t^3}} e^{-\frac{(\theta - x_0 + \theta t)^2}{4t}}. \quad (\text{D5})$$

Although the integration with respect to x_0 in Eq. (D5) could be performed analytically, it results in a lengthy combination of error functions which neither provides any further insight nor an advantage in the numeric evaluation of the integral with respect to t .

The improved approximation obtained from Eqs. (D1) and (D5) is shown in Fig. 8 (red solid line) and compared to the simple approximation from the main text (black dashed line). Although the new approximation slightly overestimates the detection rate for low thresholds and underestimates at high thresholds, it is much closer to the numerical simulations [filled circles, same data as Fig. 5(b)].

As shown in the main text in Figs. 5(b) and 5(c), a rigid shift in the argument of the original sampling approximation yields a good agreement with the measured detection rate. We note that $\gamma(\theta, x_0)$ falls rather rapidly as a function of x_0 around a value $\approx \theta - \lambda$, which does not strongly depend on θ . Hence, a Heaviside function $H[(\theta - \lambda) - x_0]$ could be used in Eq. (D2) in place of the factor $\gamma(\theta, x_0)$ to approximate the integral. Replacing $\gamma(\theta, x_0)$ with such a Heaviside function in Eq. (D2) is equivalent to a static shift by λ in the argument of the function $p_0(\theta)$ of the original sampling approximation Eq. (21), which gives a possible explanation of why shifting the sampling approximation by a fixed amount leads to a good agreement with the numerical simulations.

-
- [1] J. L. Lawson and G. E. Uhlenbeck, *Threshold Signals* (McGraw-Hill, New York, 1950).
- [2] J. A. Swets, *Science* **240**, 1285 (1988).
- [3] S. M. Kay, *Fundamentals of Statistical Signal Processing: Volume II, Detection Theory* (Prentice-Hall PTR, Upper Saddle River, NJ, 1998).
- [4] N. A. Macmillan and C. D. Creelman, *Detection Theory: A User's Guide* (Psychology Press, New York, 2004).
- [5] B. C. Levy, *Principles of Signal Detection and Parameter Estimation* (Springer Science & Business Media, Cham, 2008).
- [6] W. W. Peterson and T. G. Birdsall, The theory of signal detectability, Tech. Rep. No. 13, Electronic Defense Group, Engineering Research Institute (Department of Electrical Engineering, University of Michigan, 1953).
- [7] S. Thurner, M. C. Feurstein, S. B. Lowen, and M. C. Teich, *Phys. Rev. Lett.* **81**, 5688 (1998).
- [8] G. McCaffery, T. M. Griffith, K. Naka, M. P. Frennaux, and C. C. Matthai, *Phys. Rev. E* **65**, 022901 (2002).
- [9] V. Galdi, V. Pierro, and I. M. Pinto, *Phys. Rev. E* **57**, 6470 (1998).
- [10] A. Dari, L. Bosi, and L. Gammaitoni, *Phys. Rev. E* **81**, 011115 (2010).
- [11] N. Sharafi, M. Timme, and S. Hallerberg, *Phys. Rev. E* **96**, 032220 (2017).
- [12] J. Tiana-Alsina, C. Quintero-Quiroz, M. C. Torrent, and C. Masoller, *Phys. Rev. E* **99**, 022207 (2019).
- [13] F. S. Chance, *J. Neurophysiol.* **97**, 1799 (2007).
- [14] G. D. Mitsis, A. S. French, U. Höger, S. Courellis, and V. Z. Marmarelis, *Biol. Cybern.* **96**, 113 (2007).
- [15] R. V. Nunes, M. B. Reyes, and R. Y. de Camargo, *Biol. Cybern.* **113**, 309 (2019).
- [16] B. Fischer, A. Schander, A. K. Kreiter, W. Lang, and D. Wegener, *J. Neurophysiol.* **122**, 1634 (2019).
- [17] J. R. Holliday, J. B. Rundle, D. L. Turcotte, W. Klein, K. F. Tiampo, and A. Donnellan, *Phys. Rev. Lett.* **97**, 238501 (2006).
- [18] J. B. Rundle, J. R. Holliday, W. R. Graves, D. L. Turcotte, K. F. Tiampo, and W. Klein, *Phys. Rev. E* **86**, 021106 (2012).
- [19] A. Freking, M. Biehl, C. Braun, W. Kinzel, and M. Meesmann, *Phys. Rev. E* **60**, 5926 (1999).
- [20] T. Martin, B. Ball, and M. E. J. Newman, *Phys. Rev. E* **93**, 012306 (2016).

- [21] W. Viles, C. E. Ginestet, A. Tang, M. A. Kramer, and E. D. Kolaczyk, *Phys. Rev. E* **93**, 052301 (2016).
- [22] D. Witthaut, M. Rohden, X. Zhang, S. Hallerberg, and M. Timme, *Phys. Rev. Lett.* **116**, 138701 (2016).
- [23] D. Bernardi and B. Lindner, *Phys. Rev. Lett.* **118**, 268301 (2017).
- [24] D. Bernardi, Ph.D. thesis, Humboldt-Universität zu Berlin, 2019.
- [25] N. Arnaud, M. Barsuglia, M.-A. Bizouard, V. Brisson, F. Cavalier, M. Davier, P. Hello, S. Kreckelbergh, E. K. Porter, and T. Pradier, *Phys. Rev. D* **67**, 062004 (2003).
- [26] A. Eleuteri, L. Milano, R. De Rosa, F. Garufi, F. Acernese, F. Barone, L. Giordano, and S. Pardi, *Phys. Rev. D* **73**, 122004 (2006).
- [27] H. J. Pletsch and B. Allen, *Phys. Rev. Lett.* **103**, 181102 (2009).
- [28] R. Shannon, *Bell Syst. Tech. J.* **27**, 379 (1948).
- [29] N. Brunel and S. Sergi, *J. Theor. Biol.* **195**, 87 (1998).
- [30] R. Moreno-Bote and N. Parga, *Phys. Rev. Lett.* **92**, 028102 (2004).
- [31] K. Fisch, T. Schwalger, B. Lindner, A. Herz, and J. Benda, *J. Neurosci.* **32**, 17332 (2012).
- [32] S. E. Norman, R. J. Butera, and C. C. Canavier, *J. Neurophysiol.* **116**, 1189 (2016).
- [33] A. Lerchner, C. Ursta, J. Hertz, M. Ahmadi, P. Ruffiot, and S. Enemark, *Neural Comput.* **18**, 634 (2006).
- [34] B. Dummer, S. Wieland, and B. Lindner, *Front. Comput. Neurosci.* **8**, 104 (2014).
- [35] S. Wieland, D. Bernardi, T. Schwalger, and B. Lindner, *Phys. Rev. E* **92**, 040901(R) (2015).
- [36] S. Vellmer and B. Lindner, *Phys. Rev. Res.* **1**, 023024 (2019).
- [37] G. E. Uhlenbeck and L. S. Ornstein, *Phys. Rev.* **36**, 823 (1930).
- [38] M. C. Wang and G. E. Uhlenbeck, *Rev. Mod. Phys.* **17**, 323 (1945).
- [39] H. Risken, *The Fokker-Planck Equation* (Springer, Berlin, 1984).
- [40] C. W. Gardiner, *Handbook of Stochastic Methods* (Springer-Verlag, Berlin, 1985).
- [41] R. Stratonovich, *Topics on the Theory of Random Noise*, Vol. 2 (Gordon & Breach, New York, 1963).
- [42] M. Abramowitz and I. A. Stegun, *Handbook of Mathematical Functions* (Dover, New York, 1972).
- [43] L. M. Ricciardi, *Diffusion Processes and Related Topics on Biology* (Springer-Verlag, Berlin, 1977).
- [44] A. V. Holden, *Models of the Stochastic Activity of Neurones* (Springer-Verlag, Berlin, 1976).
- [45] H. E. Plesser, Ph.D. thesis, Universität Göttingen, 1999.
- [46] M. J. Richardson, *Biol. Cybern.* **99**, 381 (2008).
- [47] D. A. Darling and A. J. F. Siegert, *Ann. Math. Stat.* **24**, 624 (1953).
- [48] B. Lindner, *Coherence and Stochastic Resonance in Nonlinear Dynamical Systems* (Logos-Verlag, Berlin, 2002).
- [49] D. Bernardi and B. Lindner, *Phys. Rev. E* **99**, 032304 (2019).
- [50] P. Jung and H. Risken, *Phys. Lett. A* **103**, 38 (1984).
- [51] M. I. Dykman, D. G. Luchinsky, P. V. E. McClintock, N. D. Stein, and N. G. Stocks, *Phys. Rev. A* **46**, R1713 (1992).
- [52] J. Feng and B. Tirozzi, *Phys. Rev. E* **61**, 4207 (2000).
- [53] P. Lansky and L. Sacerdote, *Phys. Lett. A* **285**, 132 (2001).
- [54] A. Nikitin, N. G. Stocks, and R. P. Morse, *Phys. Rev. E* **75**, 021121 (2007).
- [55] A. Nikitin, I. A. Khovanov, R. P. Morse, and N. G. Stocks, *Eur. Phys. J.: Spec. Top* **187**, 205 (2010).
- [56] D. Bernardi, G. Doron, M. Brecht, and B. Lindner, bioRxiv (2020), <https://www.biorxiv.org/content/early/2020/03/30/2020.03.30.016261>.
- [57] J. B. Rundle and W. Klein, *J. Stat. Phys.* **72**, 405 (1993).
- [58] R. C. Merton, *J. Finance* **29**, 449 (1974).
- [59] S. G. Hanson, M. H. Pesaran, and T. Schuermann, *J. Empir. Finance* **15**, 583 (2008).
- [60] W. Gerstner, W. M. Kistler, R. Naud, and L. Paninski, *Neuronal Dynamics: From Single Neurons to Networks and Models of Cognition* (Cambridge University Press, Cambridge, UK, 2014).
- [61] T. M. Lenton, H. Held, E. Kriegler, J. W. Hall, W. Lucht, S. Rahmstorf, and H. J. Schellnhuber, *Proc. Natl. Acad. Sci. USA* **105**, 1786 (2008).
- [62] L. Gammaitoni, P. Hänggi, P. Jung, and F. Marchesoni, *Rev. Mod. Phys.* **70**, 223 (1998).
- [63] L. Gammaitoni, *Phys. Rev. E* **52**, 4691 (1995).
- [64] P. Jung, *Phys. Lett. A* **207**, 93 (1995).
- [65] F. Apostolico, L. Gammaitoni, F. Marchesoni, and S. Santucci, *Phys. Rev. E* **55**, 36 (1997).
- [66] N. G. Stocks, *Phys. Rev. Lett.* **84**, 2310 (2000).
- [67] N. G. Stocks, *Phys. Rev. E* **63**, 041114 (2001).
- [68] R. Benzi, A. Sutera, and A. Vulpiani, *J. Phys. A: Math. Gen.* **14**, L453 (1981).
- [69] L. Gammaitoni, F. Marchesoni, E. Menichella-Saetta, and S. Santucci, *Phys. Rev. Lett.* **62**, 349 (1989).
- [70] M. I. Dykman, R. Mannella, P. V. E. McClintock, and N. G. Stocks, *Phys. Rev. Lett.* **65**, 2606 (1990).
- [71] R. P. Croce, T. Demma, V. Galdi, V. Pierro, I. M. Pinto, and F. Postiglione, *Phys. Rev. E* **69**, 062104 (2004).
- [72] M. D. McDonnell and N. G. Stocks, *Phys. Rev. Lett.* **101**, 058103 (2008).
- [73] A. P. Nikitin, N. G. Stocks, R. P. Morse, and M. D. McDonnell, *Phys. Rev. Lett.* **103**, 138101 (2009).
- [74] B. Lindner and L. Schimansky-Geier, *Phys. Rev. Lett.* **86**, 2934 (2001).
- [75] G. Silberberg, M. Bethge, H. Markram, K. Pawelzik, and M. Tsodyks, *J. Neurophysiol.* **91**, 704 (2004).
- [76] C. Boucsein, T. Tetzlaff, R. Meier, A. Aertsen, and B. Naundorf, *J. Neurosci.* **29**, 1006 (2009).
- [77] V. Giorno, A. G. Nobile, and L. M. Ricciardi, *Adv. Appl. Probab.* **22**, 883 (1990).
- [78] R. G. Jáimez, P. Román, and F. T. Ruiz, *J. Appl. Prob.* **32**, 635 (1995).
- [79] R. Gutiérrez, L. M. Ricciardi, P. Román, and F. Torres, *J. Appl. Prob.* **34**, 623 (1997).
- [80] W. Braun, R. Thul, and A. Longtin, *Phys. Rev. E* **95**, 052127 (2017).
- [81] B. Lindner, *J. Stat. Phys.* **117**, 703 (2004).
- [82] B. Lindner and A. Longtin, *J. Theor. Biol.* **232**, 505 (2005).
- [83] G. Waldner, Master's thesis, Humboldt University Berlin, 2018.
- [84] H. Buchholz, *Die konfluente hypergeometrische Funktion mit besonderer Berücksichtigung ihrer Anwendungen* (Springer-Verlag, Berlin, 1953).
- [85] D. Cox and H. Miller, *The Theory of Stochastic Processes* (Wiley, New York, 1966).
- [86] S. Karlin and H. Taylor, *A First Course in Stochastic Processes* (Academic Press, New York, 1975).